Nano Res. 2011, 4(7): 695–704
DOI 10.1007/s12274-011-0125-x
Research Article

ISSN 1998-0124
CN 11-5974/O4

Controllable Synthesis of Co_3O_4 from Nanosize to Microsize with Large-Scale Exposure of Active Crystal Planes and Their Excellent Rate Capability in Supercapacitors Based on the Crystal Plane Effect

Yu Wang (✉), Ziyi Zhong, Yang Chen, Cheng Theng Ng, and Jianyi Lin

Institute of Chemical and Engineering Sciences, 1 Pesek Road, Jurong Island, Singapore 627833

Received: 11 October 2010 / Revised: 3 March 2011 / Accepted: 4 March 2011

ABSTRACT

Co_3O_4 nanorods, nanobelts, nanosheets and cubic/octahedral nanoparticles have been successfully synthesized with tunable size from the nanoscale to the microscale, accompanied by a variation in the nature of the exposed crystal planes. The products are formed by thermal treatment of $Co(CO_3)_{0.5}(OH)\cdot 0.11H_2O$ nanorod, nanobelt, nanosheet and nanocubic/nanooctahedral precursors at 250 °C. Detailed characterization, including X-ray diffraction (XRD), scanning electron microscopy (SEM), transmission electron microscopy (TEM), X-ray photoelectron spectroscopy (XPS), and nitrogen adsorption and desorption isotherms, revealed that the as-prepared nanorods, nanobelts, and nanosheet Co_3O_4 samples are single crystalline and mesoporous in nature with a predominance of exposed high-energy $(1\bar{1}0)$ crystal planes. They exhibited excellent electrochemical properties in supercapacitors, showing higher capacitance and better rate capability than conventional cubic/octahedral Co_3O_4 nanoparticles having exposed low-energy (100) and (111) planes. No decay in capacitance was observed when the scan rate was increased from 5 mV/s to 100 mV/s, or from 1 A/g to 10 A/g. The maximum value of the specific capacitance was calculated to be 162.8 F/g and the capacitance retention reached as high as 90%. Their excellent performance in supercapacitors is believed to result from the large-area exposure of active $(1\bar{1}0)$ crystal planes. The Co_3O_4 nanosheets showed the best performance due to their larger surface area and ability to provide a better pathway for charge transfer, and are promising electrode materials for application in practical supercapacitors.

KEYWORDS

Co_3O_4, mesoporous, single crystal, energy storage, supercapacitors

1. Introduction

The controllable and selective synthesis of nanostructured materials is gradually becoming more important due to their unique applications [1–7], especially in the field of catalysis [1–4]. Among the factors influencing the catalytic reactivity, selectivity and durability, the arrangement of surface atoms and number of dangling bonds on the different crystal planes are believed to be the most important [8–10], as the amount of active sites is highly dependent on these factors. Compared with materials with conventional

Address correspondence to wang_yu@ices.a-star.edu.sg, prospectwy@gmail.com

nanoparticulate forms, nanocrystals with predominant exposure of specific crystal planes show significantly higher activity and remarkable selectivity [1–4, 8–10]. Most recently, it has been shown that $(1\bar{1}0)$ and $(\bar{1}12)$ planes and their equivalent crystal planes in spinel Co_3O_4 present more active Co^{3+} sites and more open space for the absorption of CO and CH_4 molecules, hence exhibiting higher efficiency in the catalysis of CO oxidation and CH_4 combustion compared to other Co_3O_4 nanoparticles [8, 9]. In addition to catalysis, electrochemical reactions may be another important class of process that is strongly dependent on the surface structure [11, 12]. Nanostructured materials with exposed high-energy crystal planes will show distinct and novel electrochemical properties, because crystal planes with much higher energies will reduce the oxidation–reduction gaps so as to considerably accelerate the reaction rates. In this respect, it would be reasonable to expect these materials to have a good rate capability.

Among all the devices utilized in electrochemical energy storage, supercapacitors are attracting intense interest from researchers all over the world due to their unique advantages in actual applications [13–17], such as lower cost, longer lifespan, and significantly higher charging/discharging currents. There has been considerable progress in the field of supercapacitors and many highly efficient materials, including RuO_2 [16] and MnO_2 [17], have been exploited in an attempt to increase the performance in electrochemical tests. However, there have been few reports involving the study of the dependence of electrochemical effects on the different exposed crystal planes of materials. Furthermore, Co_3O_4 has been rarely investigated as a potential candidate for the electrode material in supercapacitors. Regarding the controllable synthesis of its nanostructures [18–20], only a few reports have involved the exposure of high-energy crystal planes. Developing a universal method for the preparation of functionalized Co_3O_4 still remains a significant challenge, and investigation of the electrochemical effects associated with different crystal planes of Co_3O_4 is also an intriguing research topic. Herein, we report a facile and general way to fabricate Co_3O_4 with uniform, tailorable morphologies and structures ranging from nanosize to microsize. The precursor employed to prepare the samples is $Co(CO_3)_{0.5}(OH)\cdot 0.11H_2O$, which on thermal treatment is transformed into spinel Co_3O_4. Electrochemical characterization showed that the samples exhibit excellent rate capabilities and good capacitances. To the best of our knowledge, this is the first report of the attainment of high capacitance by tailoring the crystal planes of materials. Since electrochemical energy storage is becoming more important, the as-prepared materials are promising candidates for use in the supercapacitors of the future.

2. Experimental

The following materials were used directly without further purification: ethylene glycol (EG) (Fisher Chemical, 99.99%), aqueous ammonia ($NH_3\cdot H_2O$, 28 wt%–30 wt%, J. T. Baker), cobalt nitrate ($Co(NO_3)_2$, 99.9%, Aldrich), sodium carbonate (Na_2CO_3, 99.9%, Aldrich).

In a typical synthesis, 12.5 mL of aqueous ammonia (28 wt%–30 wt%) was first mixed with 20 mL of EG and formed a homogeneous solution after 2 min of stirring. 5 mL of aqueous sodium carbonate solution (1 mol/L) was then added to the mixture which was stirred for another 2 min. Afterwards, 5 mL of aqueous cobalt nitrate solution (1 mol/L) was added to the mixture followed by continuous stirring for 20 min. The resulting homogeneous solution was transferred into a Teflon-lined stainless steel autoclave with a volume of 45 mL which was then heated in a temperature-preset oven at 170 ℃ for 17 h. The autoclave was then allowed to cool down naturally to room temperature, and the precipitate was centrifuged and rinsed with deionized water at least four times and then once with ethanol. The products were then dried in a vacuum oven overnight at 40 ℃ and calcined in a program-controlled furnace at 250 ℃ for 4 h with a ramp rate of 1 ℃/m.

The amounts of precursors required for the synthesis of the various samples were as follows.

G1-$Co(CO_3)_{0.5}(OH)\cdot 0.11H_2O$ nanorods: 12.5 mL of ammonia, 20 mL of EG, 1 mL of aqueous sodium carbonate solution (1 mol/L), 5 mL of aqueous cobalt nitrate solution (1 mol/L).

G2-$Co(CO_3)_{0.5}(OH)\cdot 0.11H_2O$ nanobelts: 12.5 mL of ammonia, 20 mL of EG, 1.2 mL of aqueous sodium

carbonate solution (1 mol/L), 5 mL of aqueous cobalt nitrate solution (1 mol/L).

G3-$Co(CO_3)_{0.5}(OH)\cdot 0.11H_2O$ nanosheets: 10 mL of ammonia, 25 mL of EG, 1.5 mL of aqueous sodium carbonate solution (1 mol/L), 5 mL of aqueous cobalt nitrate solution (1 mol/L).

Co_3O_4 cubic/octahedral nanoparticles: 12.5 mL of ammonia, 12.5 mL of deionized water, 5 mL of aqueous cobalt nitrate solution (1 mol/L).

Electrochemical characterization: 10 mg of a sample was mixed with 2 mL of a solution composed of 85% deionized water, 10% 2-propanol and 5% Nafion by volume. The mixture was converted into a homogeneous solution by vigorous stirring for 3 h. 10 μL of this mixture was extracted by micropipette and dropped onto a graphite electrode to serve as the working electrode after being dried naturally in air. The electrochemical properties of the sample were tested using an Autolab potentiostat (model AUT71740) in a three-electrode cell. Pt foil was used as the counter electrode, with Ag/AgCl as the reference electrode and KOH (2 mol/L) as the electrolyte.

3. Results and discussion

3.1 Characterization of Co_3O_4 nanostructured materials

Figures 1(a), 1(c), and 1(d) show some representative low-magnification transmission electron microscopy (TEM) images of $Co(CO_3)_{0.5}(OH)\cdot 0.11H_2O$ nanorods (G1), nanobelts (G2) and nanosheets (G3), respectively, in which uniform products can be clearly observed. All of these samples exhibit sharp and straight sides with ribbon (Fig. 1(a)), belt (Fig. 1(c)) or sheet-shaped (Fig. 1(d)) morphologies. By changing the concentrations of the precursors, the widths of the products were tailored from 15 nm (Fig. 1(a)) to 30 nm (Fig. 1(c)), and to approximately 1.50 μm (Fig. 1(d)). Meanwhile, their lengths could be varied from 250 nm (Fig. 1(a)) to 800 nm (Fig. 1(c)), and finally up to more than 1 μm (Fig. 1(d)). Another important discovery is that the products are single crystalline, as highlighted in the high-resolution transmission electron microscopy (HRTEM) image (Fig. 1(b)) collected from the marked

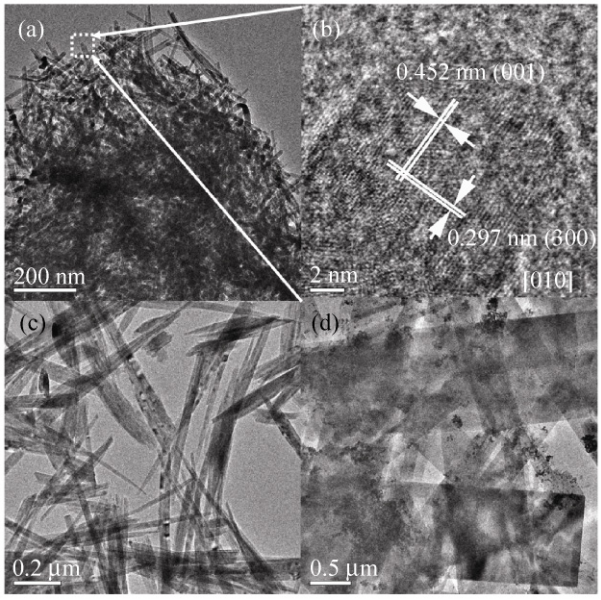

Figure 1 TEM and HRTEM images for the as-prepared $Co(CO_3)_{0.5}(OH)\cdot 0.11H_2O$ samples: (a) TEM image of nanorods; (b) HRTEM image of nanorods; (c) TEM image of nanobelts (d) TEM image of nanosheets

area in Fig. 1(a). The distances between adjacent crystal planes are 0.452 nm and 0.297 nm, corresponding to the interplanar spacings (001) and (300), respectively.

As shown in Fig. 2(a), all the XRD patterns from samples labeled as G1, G2, and G3 can be indexed as orthorhombic $Co(CO_3)_{0.5}(OH)\cdot 0.11H_2O$, with lattice constants of a = 0.8792 nm, b = 1.0150 nm, and c = 0.4433 nm (JCPDS card No. 48-0083), with no evidence of impurity peaks from any other phases. After calcination of the samples at 250 ˚C for 4 h in air with a ramp rate of 1 ˚C/min, the XRD patterns of the products (Fig. 2(b)) indicated that the materials had undergone partial oxidation of Co^{2+} into Co^{3+}, leading to the formation of a pure spinel Co_3O_4 face-centered cubic (fcc) phase with a lattice constant of a = 0.8084 nm (JCPDS card No. 42-1467).

Transmission electron microscopy (TEM) and HRTEM observations confirmed the conversion process, as shown in Fig. 3. Figures 3(a), 3(c), and 3(d) show some representative TEM images of materials S1–S3 formed by calcination of G1–G3. Thermal conversion did not destroy the particle morphology but resulted in the appearance of some porous structure. The corresponding HRTEM images (Figs. 3(b), 3(d), and 3(e)) indicate lattice spacings of around 0.250 nm and

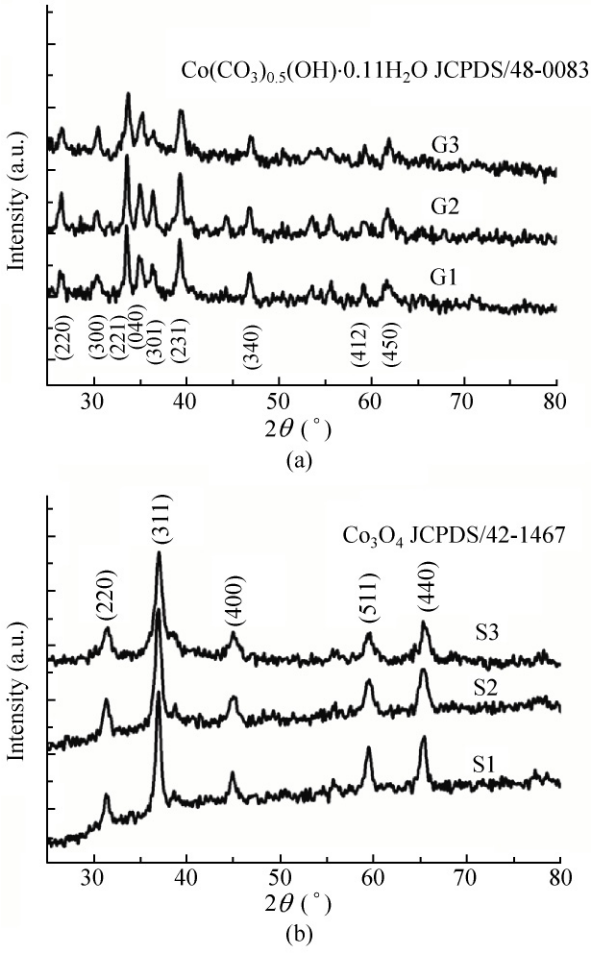

Figure 2 XRD patterns for the $Co(CO_3)_{0.5}(OH)\cdot 0.11H_2O$ nanostructures and the calcined samples: (a) $Co(CO_3)_{0.5}(OH)\cdot 0.11H_2O$ nanostructures G1–G3; (b) Co_3O_4 samples S1–S3 after calcination

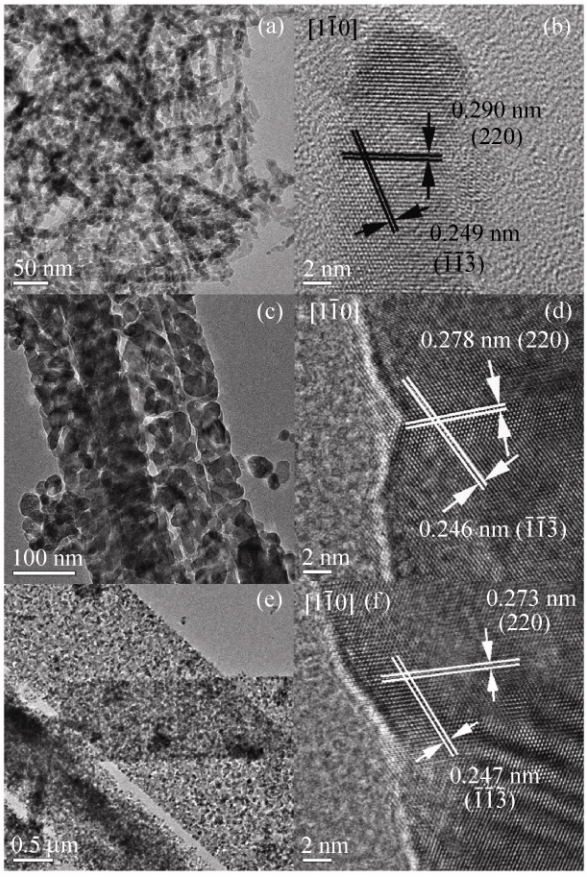

Figure 3 TEM and HRTEM micrographs of the calcined samples S1–S3: (a), (b) Co_3O_4 nanorods S1; (c), (d) Co_3O_4 nanobelts, S2; (e), (f) Co_3O_4 nanosheets, S3

0.280 nm, which are in good agreement with the standard data of {113} and {220} interplanar spacings for spinel Co_3O_4. In addition, based on the structural analysis, the normal directions perpendicular to the particle surfaces can be indexed as [1$\bar{1}$0] and [110]. Therefore, the preferentially exposed crystal planes for these samples, including two side planes and two end planes, can be determined to be {110}. It is noteworthy that as the particle widths increase from S1 to S3, the exposed {110} planes account for an increasing proportion of the total surface area. To the best of our knowledge, this is the first report of the successful synthesis of single crystal Co_3O_4 nanosheets with large scale exposure of unusually high-energy crystal planes. It is widely recognized that developing well-grown nanocrystals with a predominance of exposed regular and sharp crystal planes, especially those with high energy, still remains a great challenge. Further examination of the properties of our materials, especially in the field of specific catalysis, would be of interest. Our results provide a platform for the study of specific molecular absorption, desorption and even chemical reactions using atomic force microscope (AFM) and scanning tunneling microscope (STM) techniques [21, 22]. Through this approach, it should be possible to investigate the mechanisms of some significant chemical reactions at the molecular level, e.g., CO oxidation and CH_4 combustion.

In addition to X-ray diffraction (XRD) measurements, the conversion of $Co(CO_3)_{0.5}(OH)\cdot 0.11H_2O$ into Co_3O_4 can also be confirmed by using photoelectron spectroscopy (XPS) to monitor the change in oxidation state of the Co. Figures 4(a) and 4(b) show the X-ray photoelectron spectra of G1 and its calcined analogue S1. Both samples were thoroughly dried in a vacuum

oven at 40 ˚C overnight to remove adsorbed water prior to characterization. In the spectrum of S1 (Fig. 4(b)) the two XPS binding energy (BE) peaks without prominent shake-up satellite peaks, centered at 794.79 eV and 779.77 eV, can be assigned to Co $2p_{1/2}$ and Co $2p_{3/2}$ spin-orbit peaks, respectively, characteristic of Co_3O_4 [23]. The precursor sample G1 shows two highly intense shake-up satellite peaks centered at 787.24 eV and 803.23 eV, which are consistent with the presence of Co^{2+} [23]. The peaks centered at 781.22 eV and 797.21 eV, which correspond to Co $2p_{3/2}$ and Co $2p_{1/2}$ core levels, are slightly shifted to higher binding energy compared to those of the calcined sample, further confirming that the sample G1 mainly consists of Co^{2+} [24].

Figure 5(a) shows a typical low-magnification TEM image of G1 showing it consists of nanorods with a regular rectangular cross-section and lengths of 200–300 nm. In the enlarged image, shown in Fig. 5(b), it can be seen that the nanorods have a thickness of 8–10 nm and widths ranging from 14–16 nm. Upon calcination at 250 ˚C for 4 h, the resulting sample S1 maintains its 3D morphology and particle size. However, it experienced a transformation in chemical composition and crystal structure from orthorhombic $Co(CO_3)_{0.5}(OH)\cdot 0.11H_2O$ to fcc Co_3O_4. Along the [1$\bar{1}$0] and [001] directions of fcc Co_3O_4, two distinct crystal structures are revealed, as indicated in Figs. 5(c) and 5(e). They exhibit continuous crystal structures and almost completely flat planes. In the crystallographic nature of fcc Co_3O_4, the (1$\bar{1}$0) and [001] directions are perpendicular to each other. The micrographs in Figs. 5(c) and 5(e) confirm that the calcined S1 has

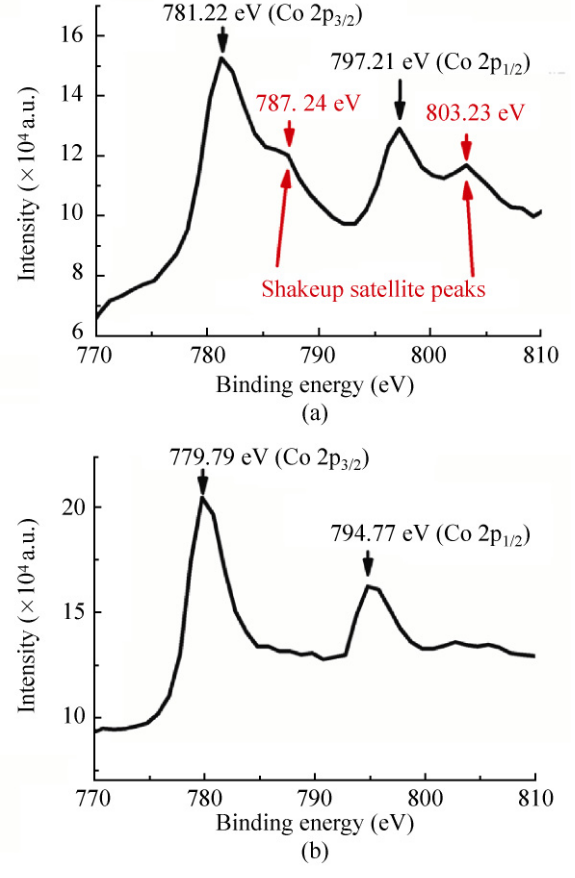

Figure 4 XPS spectra of (a) precursor G1 and (b) its calcined analogue S1

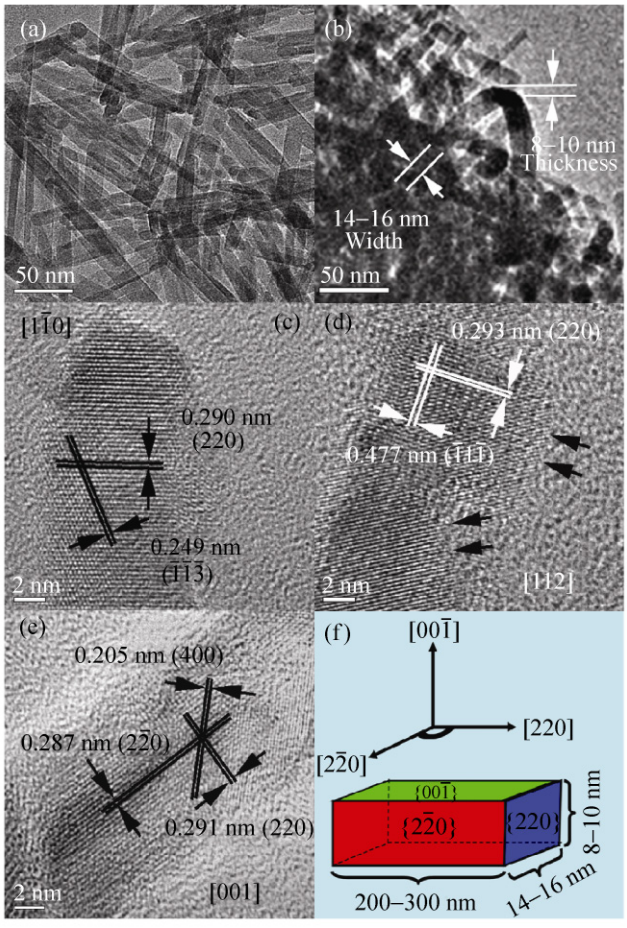

Figure 5 A representative TEM image (a) and the enlarged TEM image (b) reveal that the particles in precursor G1 have dimensions of 8–10 nm in thickness, 14–16 nm in width, and 200–300 nm in length. After calcination at 250 ˚C for 4 h to give sample S1, no apparent changes in morphology are observed (c–e). HRTEM characterization shows the crystal structure along three different directions, including [1$\bar{1}$0] (c), [$\bar{1}$12] (d) and [001] (e). All the results indicate that the calcined S1 has a cuboid morphology, with exposure of specific crystal planes (f)

retained its original nanorod shape with a rectangular cross-section, and the two exposed crystal planes being $(1\bar{1}0)$ and (001). Along another crystal orientation $[\bar{1}12]$, which is located in the plane jointly determined by $[1\bar{1}0]$ and [001], and perpendicular to [110], a third crystal structure has also been detected, as shown in Fig. 5(d), (indicated by black arrows). The SEM data provide additional proof that the calcined S1 consists of cuboid nanorods with an axial direction of [110]. The particles of calcined S1 can be described as a rod-like nanostructure with three sets of mutually perpendicular crystal planes, as illustrated in Fig. 5(f). From Fig. 5(f), the calculated percentage of the total surface area contributed by the set of high-energy planes {110} (including (110) and its equivalent plane $(1\bar{1}0)$), can reach as high as 39.2%. As the width of the nanostructure increases from S1 to S2 to S3, the percentage of the surface area contributed by the highly active planes will also increase.

3.2 Electrochemical testing of Co_3O_4

A number of samples were selected in order to investigate the relationship between the electrochemical performance and the sample morphology. Cyclic voltammetry (CV) (Fig. 6(a)) and chronopotentiograms (Fig. 6(b)) revealed that the calcined S3 exhibits higher capacitance and better rate capability than calcined S1. The maximum capacitance for a current density of 1 A/g reached as high as 176.8 F/g after 5000 cycles, which is much higher than the most recently reported value for Co_3O_4 (prepared by calcination of β-$Co(OH)_2$) of 92 F/g [25]. For a higher current density of 10 A/g, S3 was still able to retain a value of 156.0 F/g, corresponding to 88.2% of the initial specific capacitance (Fig. 6(b)). The CV curves shown in Fig. 6(a) indicate that, if a narrower potential scan range is applied, it can result in a higher specific capacitance. This is reasonable, because the enclosed area within the curve in a scan range of 0.25 V to 0.5 V is much more "effective" than that in a scan range of 0 to 0.5 V in view of the capacitance equation: $C = It/m \cdot \Delta V$, where C is the specific capacitance, I is the current density, m is the mass of the sample, and ΔV is the potential drop within the scan. However, in our experiments, which are aimed at developing potential applications, a wider scan scope ranging from 0 to 0.5 V was utilized in order to provide a more realistic test of the electrochemical performance of the samples. The two distinct redox peaks in Fig. 6(a) indicate that reversible electrochemical reactions occur during the cyclic voltammogram scanning process, and their shapes are totally different from those of normal double-layer capacitance with its typical rectangular area [16]. In Fig. 6(b), which focuses on the charging stage, two steps can be clearly detected, where double-layer capacitance and pseudocapacitance have the distinctive characteristics of being parallel to the voltage axis and the slope, respectively. Two kinds of capacitive mechanism are involved: (1) charge separation for double-layer capacitance and electrochemical absorption–desorption; (2) redox reactions for the pseudocapacitance. The data shown in Figs. 6(a) and 6(b) indicate that no apparent decay takes place when the scan rate is increased to 100 mV/s. This result can be ascribed to the large exposure of high-energy crystal planes in the sample, since it is well known that the high-energy crystal planes ((110) or its equivalent planes) can speed up surface reactions. From the results of the nitrogen adsorption and desorption isotherm measurements, the Brunauer–Emmett–Teller (BET) surface area and pore diameter of calcined S3 were determined to be 127.4 m^2/g and 2.3–2.7 nm respectively, as shown in Fig. 6(c). These values should be compared with those in the literature for Co_3O_4 prepared by calcination of β-$Co(OH)_2$ [25], namely a surface area of 25.12 m^2/g and pore size of 23.5 nm. The larger surface area of our material is responsible for its higher capacitance, because surface area is one of the key factors affecting the interfacial electrochemical properties of a material.

The capacitive properties of calcined S1 were also investigated. The CV curves (Fig. 6(d)) and chronopotentiograms (Fig. 6(e)), are fairly similar to those for calcined sample S1 (Figs. 6(a) and 6(b)), and the material demonstrated characteristics of both high capacitance and good rate capability. The high surface area, as indicated in Fig. 6(f) (90.6 m^2/g), is responsible for the high specific capacitance, just as for the calcined S3. It is noteworthy that the calcined S3, with its sheet-shaped structure, showed a superior performance in electrochemical tests to the rod-like structure (calcined S1). In electrochemical systems, at least three factors may be responsible for an enhanced performance,

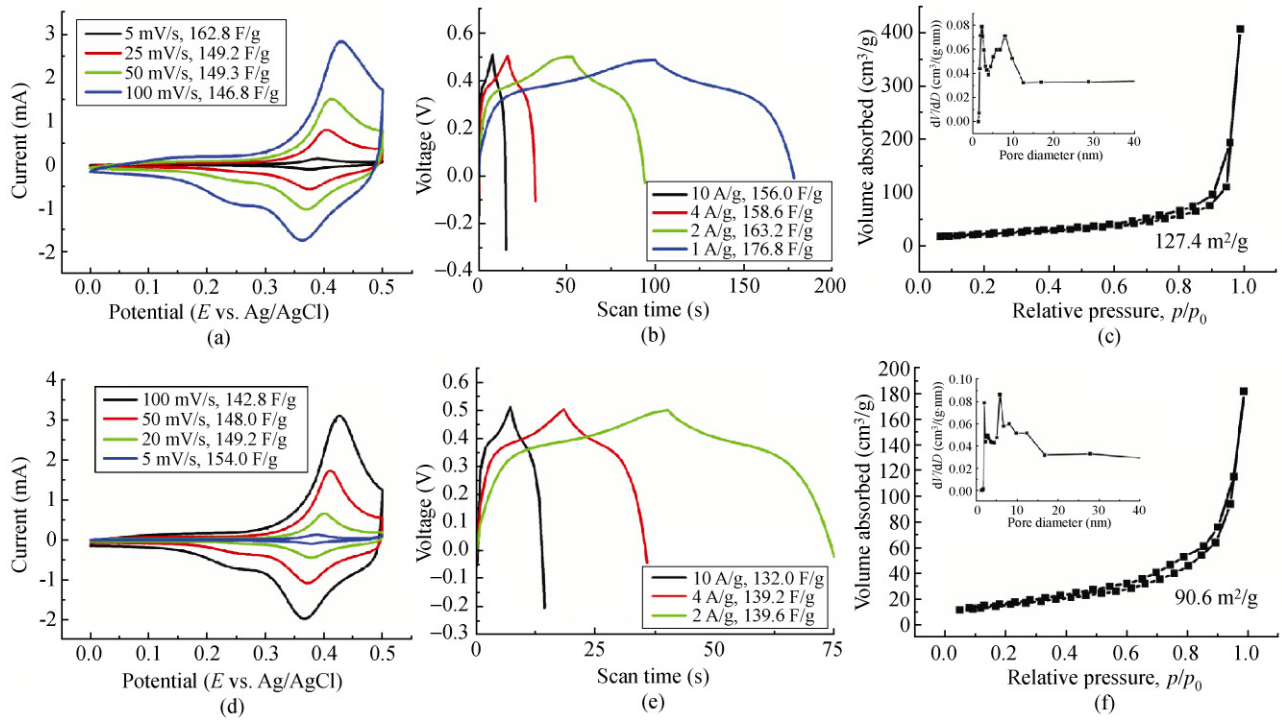

Figure 6 Electrochemical characterization and BET measurements on the calcined S3 (a–c) and S1 (d–f)

namely the surface area, conductivity and electrolyte diffusion efficiency. In general, a larger surface area will result in the improvement of the contact area between electrode and electrolyte, leading to better conductivity and more efficient diffusion of electrolyte, giving an accelerated charge transfer rate and ultimately improve the performance. In other electrochemical systems, e.g., Li-ion batteries [26, 27], it has been shown that a belt-or sheet-shaped structures are more favorable in terms of providing an efficient pathway for charge transfer than a rod-like one. Calcined sample S2 exhibits values of surface area (118.7 m^2/g) and pore sizes (from 2.8–6.0 nm) (see Fig. S-1 in the Electronic Supplementary Material (ESM)) which fall in the range between the values for S1 and S3, and its electrochemical performance, including capacitance and rate capability, is also intermediate between those of S1 and S3. A reversible capacitance of 150–160 F/g was found for S2 (see Fig. S-1 in the ESM). This is reasonable, since all the three samples have high-energy crystal planes of (110) exposed to a large extent and the percentage of the whole surface area accounted for by (110) planes increases with the sample width. Although some materials have previously been shown to exhibit better performance than Co_3O_4 in supercapacitors, e.g., NiO and $NiCo_2O_4$ [28, 29], our results are still high enough for the materials to be employed in practical supercapacitors.

Co_3O_4 nanocrystals with cubic and octahedral morphology were also used as control samples in electrochemical tests in order to investigate the crystal plane effect. SEM (Fig. 7(a)) and TEM (Fig. (b)) images indicate that the samples consist of uniform Co_3O_4 nanocrystals with a diameter of 10–15 nm, most of which exhibit nanocube or nanooctahedron shapes, implying that the samples expose their (100) or (111) crystal planes [18–20]. BET analysis reveals that these nanocrystals had a surface area of 51.86 m^2/g (Fig. 7(c)). A series of electrochemical tests, including CV (Fig. 7(d)) and chronopotentiograms (Fig. 7(e)), showed that the maximum specific capacitance was only 20 F/g under a slow scan rate of 5 mV/s (Fig. 7(d)), which is much lower than the values for the calcined S1, S2, and S3. In addition, chronopotentiograms (Fig. 7(e)) also show a poor specific capacitance of 17.4 F/g under a low constant current flow of 0.1 A/g. Furthermore, the rate capability is not ideal. In Fig. 7(f), it can be seen that the specific capacitance decays rapidly with increasing

scan rate, and a loss of nearly 50% occurs at a scan rate of 150 mV/s. It has been reported that the (100) and (111) crystal planes of Co_3O_4 are catalytically very inactive compared to (110) [8–10]. Since electrochemical testing is also based on an interfacial reaction process, it is easily understood why the Co_3O_4 nanocrystals demonstrate a much poorer performance in the electrochemical tests, even though its surface area is as high as 51.86 m^2/g (Fig. 7(c)).

In general, there are some aspects we should consider in order to improve the electrochemical performance for supercapacitors, namely the double layer capacitance, faradaic capacitance from surface redox process and faradaic contribution from the diffusion-dominated interaction between electrolyte ions and electrode materials [30–32]. For some layered or other materials which possess interior sites which can accommodate active species—especially when they exhibit mesoporous structures—active ions, e.g., Li, can insert/deinsert into the bulk electrode materials so that the

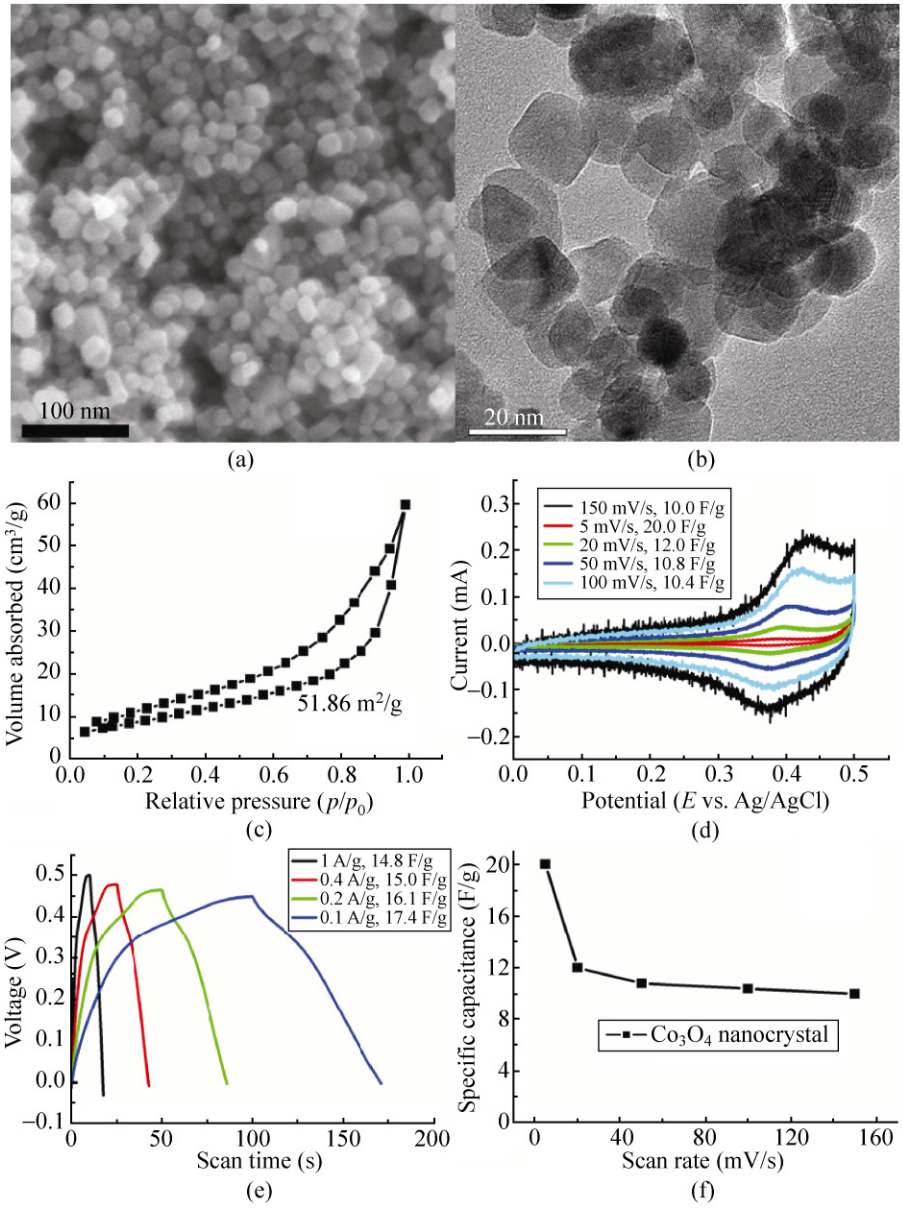

Figure 7 Characterization of Co_3O_4 nanocrystals used as a control in electrochemical tests—SEM image (a), TEM image (b), BET measurements (c)—and the results of the electrochemical tests (d–f)

related energy density will be significantly increased [30]. In fact, the process is similar to that in the cathodes of Li-based batteries where intercalation and deintercalation of Li ions usually occur, although we still define such systems as supercapacitors. However, the definition further blurs the differentiation between supercapacitors and batteries. In the CV profiles in Figs. 6(a), 6(d), and 7(d), a pair of redox processes give rise to the anodic (around 0.42 V, versus Ag/AgCl) and cathodic (around 0.37 V, versus Ag/AgCl) peaks. The tiny difference between them (around 0.05 V) implies that the polarization is greatly reduced and that the electrolyte diffusion process will play a less important role in the overall capacitive performance [33, 34]. For nanobelts/nanosheets or nanoparticles, such a result can be reasonably understood, because these two-dimensional or zero-dimensional samples present ultrathin thickness and mesoporosity, or small size, so that the electrolyte can easily diffuse through them without an internal pressure and delay effect [34], which also can further explain the good rate capability achieved for our nanobelt/nanosheet samples.

4. Conclusions

The controllable synthesis of Co_3O_4 nanostructures with different exposed crystal planes has been achieved. The as-made samples exhibited large scale exposure of the set of high-energy {110} crystal planes of (at least 39.2%). A series of electrochemical tests revealed that the as-prepared samples exhibited higher capacitance and better rate capability compared to conventional Co_3O_4 nanocubes/nanooctahedra displaying lower energy (100) and (111) crystal planes, and can be employed in practical supercapacitors; other applications in areas such as Li-ion batteries and chemical sensing are also possible. Furthermore, the large scale exposure of high-energy crystal planes and its quantification provide good opportunities for researchers to study specific catalysis processes, such as CO oxidation, N_2O decomposition and CH_4 combustion, using these materials.

Acknowledgements

This research was financially supported by the Agency for Science, Technology, and Research (ASTAR) in Singapore.

Electronic Supplementary Material: Supplementary material (galvanostatic and BET measurements for Co_3O_4 nanobelts) is available in the online version of this article at http://dx.doi.org/10.1007/s12274-011-0125-x.

References

[1] Bratlie, K. M.; Kliewer, C. J.; Somorjai, G. A. Structure effects of benzene hydrogenation studied with sum frequency generation vibrational spectroscopy and kinetics on Pt(111) and Pt(100) single-crystal surfaces. *J. Phys. Chem. B* **2006**, *110*, 17925–17930.

[2] Tian, N.; Zhou, Z. Y.; Sun, S. G.; Ding, Y.; Wang, Z. L. Synthesis of tetrahexahedral platinum nanocrystals with high-index facets and high electro-oxidation activity. *Science* **2007**, *316*, 732–735.

[3] Burda, C.; Chen, X.; Narayanan, R.; El-Sayed, M. A. Chemistry and properties of nanocrystals of different shapes. *Chem. Rev.* **2005**, *105*, 1025–1102.

[4] Si, R.; Flytzani-Stephanopoulos, M. Shape and crystal-plane effects of nanoscale ceria on the activity of Au–CeO_2 catalysts for the water–gas shift reaction. *Angew. Chem. Int. Ed.* **2008**, *47*, 2884–2887.

[5] Tao, A. R.; Habas, S.; Yang, P. D. Shape control of colloidal metal nanocrystals. *Small* **2008**, *4*, 310–325.

[6] Wang, Y.; Liao, Q.; Lei, H.; Zhang, X. P.; Ai, X. C.; Zhang, J. P.; Wu, K. Interfacial reaction growth: Morphology, composition, and structure controls in preparation of crystalline $Zn_xAl_yO_z$ nanonets. *Adv. Mater.* **2006**, *18*, 943–947.

[7] Zhu, M.; Aikens, C. M.; Hollander, F. J.; Schatz, G. C.; Jin, R. C. Correlating the crystal structure of a thiol-protected Au_{25} cluster and optical properties. *J. Am. Chem. Soc.* **2008**, *130*, 5883–5885.

[8] Hu, L. H.; Peng, Q.; Li, Y. D. Selective synthesis of Co_3O_4 nanocrystal with different shape and crystal plane effect on catalytic property for methane combustion. *J. Am. Chem. Soc.* **2008**, *130*, 16136–16137.

[9] Xie, X. W.; Li, Y.; Liu, Z. Q.; Haruta, M.; Shen, W. J. Low-temperature oxidation of CO catalysed by Co_3O_4 nanorods. *Nature* **2009**, *458*, 746–749.

[10] Ziókowski, J.; Barbaux, Y. Identification of sites active in oxidation of butane-1 to butadiene and CO_2 on Co_3O_4 in terms of crystallochemical model of solid surfaces. *J. Mol. Catal.* **1991**, *67*, 199–215.

[11] Sugimoto, W.; Iwata, H.; Yasunaga, Y.; Murakami, Y.;

Takasu, Y. Preparation of ruthenic acid nanosheets and utilization of its interlayer surface for electrochemical energy storage. *Angew. Chem. Int. Ed.* **2003**, *42*, 4092–4096.

[12] Choi, D.; Blomgren, G. E.; Kumta, P. N. Fast and reversible surface redox reaction in nanocrystalline vanadium nitride supercapacitors. *Adv. Mater.* **2006**, *18*, 1178–1182.

[13] Kötz, R.; Carlen, M. Principles and applications of electrochemical capacitors. *Electrochim. Acta* **2000**, *45*, 2483–2498.

[14] Burke, A. Ultracapacitors: Why, how, and where is the technology? *J. Power Sources* **2000**, *91*, 37–50.

[15] Chmiola, J.; Yushin, G.; Gorgotsi, Y.; Portet, C.; Simon, P.; Taberna, P. L. Anomalous increase in carbon capacitance at pore size below 1 nm. *Science* **2006**, *313*, 1760–1763.

[16] Wang, Y.; Foo, C. Y.; Hoo, T. K.; Ng, M.; Lin, J. Y. Designed smart system of the sandwiched and concentric architecture of RuO_2/C/RuO_2 for high performance in electrochemical energy storage. *Chem. Eur. J.* **2010**, *16*, 3598–3603.

[17] Sharma, R. K.; Oh, H. S.; Shul, Y. G.; Kim, H. Carbon-supported, nano-structured, manganese oxide composite electrode for electrochemical supercapacitor. *J. Power Sources* **2007**, *173*, 1024–1028.

[18] Xu, R.; Zeng, H. C. Self-generation of tiered surfactant superstructures for one-pot synthesis of Co_3O_4 nanocubes and their close- and non-close-packed organizations. *Langmuir* **2004**, *20*, 9780–9790.

[19] Jana, N. R.; Chen, Y. F.; Peng, X. G. Size- and shape-controlled magnetic (Cr, Mn, Fe, Co, Ni) oxide nanocrystals via a simple and general approach. *Chem. Mater.* **2004**, *16*, 3931–3935.

[20] He, T.; Chen, D. R.; Jiao, X. L.; Wang, Y. L.; Duan, Y. Z. Solubility-controlled synthesis of high-quality Co_3O_4 nanocrystals. *Chem. Mater.* **2005**, *17*, 4023–4030.

[21] Wang, Y. F.; Ye, Y. C.; Wu, K. Adsorption and assembly of copper phthalocyanine on cross-linked TiO_2(110)-(1×2) and TiO_2(210). *J. Phys. Chem. B* **2006**, *110*, 17960–17965.

[22] Ye, Y. C.; Sun, W.; Wang, Y. F.; Shao, X.; Xu, X. G.; Cheng, F.; Li, J. L.; Wu, K. A unified model: Self-assembly of trimesic acid on gold. *J. Phys. Chem. C* **2007**, *111*, 10138–10141.

[23] Varghese, B.; Teo, C. H.; Zhu, Y. W.; Reddy, M. V.; Bobba, V. R. C.; Chowdari, B. V. R.; Wee, A. T. S.; Tan, V. B. C.; Lim, C. T.; Sow, C. H. Co_3O_4 nanostructures with different morphologies and their field-emission properties. *Adv. Funct. Mater.* **2007**, *17*, 1932–1939.

[24] Zhuo, L. H.; Ge, J. C.; Cao, L. H.; Tang, B. Solvothermal synthesis of CoO, Co_3O_4, $Ni(OH)_2$ and $Mg(OH)_2$ nanotubes. *Cryst. Growth Des.* **2009**, *9*, 1–6.

[25] Xiong, S. L.; Yuan, C. Z.; Zhang, X. G.; Xi, B. J.; Qian, Y. T. Controllable synthesis of mesoporous Co_3O_4 nanostructures with tunable morphology for application in supercapacitors. *Chem. Eur. J.* **2009**, *15*, 5320–5326.

[26] Wang, Y.; Xia, H.; Lu, L.; Lin, J. Y. Excellent performance in lithium-ion battery anodes: Rational synthesis of $Co(CO_3)_{0.5}(OH)\cdot 0.11H_2O$ nanobelt array and its conversion into mesoporous and single-crystal Co_3O_4. *ACS Nano* **2010**, *4*, 1425–1432.

[27] Wang, Y.; Zhang, H. J.; Lu, L.; Stubbs, L. P.; Wong, C. C.; Lin, J. Y. Designed functional systems from peapod-like Co@carbon to Co_3O_4@carbon nanocomposites. *ACS Nano* **2010**, *4*, 4753–4761.

[28] Lang, J. W.; Kong, L. B.; Wu, W. J.; Luo, Y. C.; Kang, L. Facile approach to prepare loose-packed NiO nano-flakes materials for supercapacitors. *Chem. Commun.* **2008**, 4213–4215.

[29] Wei, T. Y.; Chen, C. H.; Chien, H. C.; Lu, S. Y.; Hu, C. C. A cost-effective supercapacitor material of ultrahigh specific capacitances: Spinel nickel cobaltite aerogels from an epoxide-driven sol–gel process. *Adv. Mater.* **2010**, *22*, 347–351.

[30] Brezesinski, T.; Wang, J.; Tolbert, S. H.; Dunn, B. Ordered mesoporous α-MoO_3 with iso-oriented nanocrystalline walls for thin-film pseudocapacitors. *Nat. Mater.* **2010**, *9*, 146–151.

[31] Brezesinski, T.; Wang, J.; Polleux, J.; Dunn, B.; Tolbert, S. H. Templated nanocrystal-based porous TiO_2 films for next-generation electrochemical capacitors. *J. Am. Chem. Soc*. **2009**, *131*, 1802–1809.

[32] Brezesinski, T.; Wang, J.; Senter, R.; Brezesinski, K.; Dunn, B.; Tolbert, S. H. On the correlation between mechanical flexibility, nanoscale structure, and charge storage in periodic mesoporous CeO_2 thin films. *ACS Nano* **2010**, *4*, 967–977.

[33] Wang, Y.; Zhang, H. J.; Lim, W. X.; Lin, J. Y.; Wong, C. C. Designed strategy to fabricate patterned V_2O_5 nanobelt array as superior electrodes for Li ion batteries. *J. Mater. Chem.* **2011**, *21*, 2362–2368.

[34] Lu, Q.; Mellinger, Z. J.; Wang, W. G.; Li, W. F.; Chen, Y. P.; Chen, J. G.; Xiao, J. Q. Differentiation of bulk and surface contribution to supercapacitance in amorphous and crystalline NiO. *ChemSusChem* **2010**, *3*, 1367–1370.